The Astrophysical Journal Letters, 809:L33 (6pp), 2015 August 20 doi:10.1088/2041-8205/809/2/L33

CHARACTERIZING THE ATMOSPHERES OF THE HR8799 PLANETS WITH *HST*/WFC3

Abhijith Rajan[1], Travis Barman[2], Rémi Soummer[3], J. Brendan Hagan[3,4], Jennifer Patience[1], Laurent Pueyo[3], Élodie Choquet[3], Quinn Konopacky[5], Bruce Macintosh[6], and Christian Marois[7]
[1] School of Earth and Space Exploration, Arizona State University, Tempe, AZ 85282, USA
[2] Department of Planetary Sciences and Lunar and Planetary Laboratory, University of Arizona, Tucson, AZ 85721, USA
[3] Space Telescope Science Institute, Baltimore, MD 21218, USA
[4] Purdue University, West Lafayette, IN 47907, USA
[5] Dunlap Institute for Astronomy & Astrophysics, University of Toronto, 50 St. George Street, Toronto, ON M5S 3H4, Canada
[6] Kavli Institute for Particle Astrophysics and Cosmology, Stanford University, Stanford, CA 94305, USA
[7] National Research Council of Canada Herzberg, Victoria, BC V9E 2E7, Canada
Received 2015 April 2; accepted 2015 August 3; published 2015 August 20

ABSTRACT

We present results from a *Hubble Space Telescope* (*HST*) program characterizing the atmospheres of the outer two planets in the HR8799 system. The images were taken over 15 orbits in three near-infrared (near-IR) medium-band filters—F098M, F127M, and F139M—using the Wide Field Camera 3. One of the three filters is sensitive to a water absorption band inaccessible from ground-based observations, providing a unique probe of the thermal emission from the atmospheres of these young giant planets. The observations were taken at 30 different spacecraft rolls to enable angular differential imaging (ADI), and the full data set was analyzed with the Karhunen–Loéve Image Projection routine, an advanced image processing algorithm adapted to work with *HST* data. To achieve the required high contrast at subarcsecond resolution, we utilized the pointing accuracy of *HST* in combination with an improved pipeline designed to combine the dithered ADI data with an algorithm designed to both improve the image resolution and accurately measure the photometry. The results include F127M (*J*) detections of the outer planets, HR8799b and c, and the first detection of HR8799b in the water-band (F139M) filter. The F127M photometry for HR8799c agrees well with fitted atmospheric models, resolving the longstanding difficulty in consistently modeling the near-IR flux of the planet.

Key words: brown dwarfs – planetary systems – stars: atmospheres – stars: low-mass

1. INTRODUCTION

Within the past decade, direct imaging of exoplanets has advanced from initial discoveries of favorable low-contrast planetary-mass companions like 2M1207b (Chauvin et al. 2005a) and AB Pic b (Chauvin et al. 2005b) to high-contrast exoplanets around bright young stars like the HR8799 planetary system (Marois et al. 2008, 2010), β Pic b (Lagrange et al. 2010), HD 95086b (Rameau et al. 2013), and GJ 504b (Kuzuhara et al. 2013). Directly imaged exoplanets form a critical subset of the exoplanet population for which it is possible to characterize atmospheric properties from thermal emission. Given the steep, monotonic decline in planet brightness with time (e.g., Burrows et al. 2001), the currently known directly imaged exoplanets (companions to young stars) enable investigations into the early evolution of exoplanets. Imaged young atmospheres also present a valuable comparison to the transmission (e.g., Deming et al. 2005; Sing et al. 2008) and emission (e.g., Charbonneau et al. 2005; Knutson et al. 2007) spectra of intensely irradiated planets orbiting older stars.

The *Hubble Space Telescope* (*HST*) has been successfully employed in characterizing exoplanet systems for over a decade (Charbonneau et al. 2002; Soummer et al. 2012). We present Wide Field Camera 3 imaging of the multiple planet system HR8799. The system has four young, massive planets (~4–7 $M_{\rm Jup}$) orbiting a ~30 Myr (Zuckerman et al. 2011) A5 star, amenable to both photometric and spectroscopic follow-up. This is the first time that planets with high contrasts have been successfully imaged with WFC3/IR, a camera without a coronagraph and with an undersampled point-spread function (PSF). The techniques described in the paper should enable future studies of planetary systems with *HST*. In this paper, we characterize the outer two planets, HR8799b and c, by combining the new space-based near-infrared (near-IR) photometric data to the existing suite of ground-based data available for the two planets and discuss the implications of the new photometry.

2. OBSERVATIONS

Observations for this study[8] were taken from 2011 November to 2012 December with the near-IR channel of WFC3 on the *HST*. Due to the brightness of the primary star ($J = 5.3$ mag), all combinations of sub-array and detector readout times result in a saturated zeroth read. In the absence of a coronagraph we designed the observations to saturate the central ~0.″5 of the stellar PSF using 2.2 s long observations, focusing the program on the b and c planets.

The HR8799 system was observed in three medium-band filters, F098M, F127M, and F139M, over 15 orbits. The orbits were grouped contiguously in sets of three to increase the PSF correlation. The observing sequence was designed to maximize the total roll angle and minimize variations in the PSF of the observations over the duration of the program. To maximize the rotation, the star was observed over two different roll angles in each orbit, resulting in observations taken over 30 separate roll angles covering ~270° (not uniformly sampled) to enable angular differential imaging (ADI) reduction (Marois et al. 2006). Within each roll, the telescope was dithered using a customized nine-point spiral dither pattern covering a 0.″13 × 0.″13 region, with half-pixel dithers (~64 mas), ensuring a well sampled PSF. This observing procedure

[8] GO Program #12511.

enhanced stability, but resulted in reduced total exposure time on the object and a limited range of roll angles within each block of three orbits. At the conclusion of the observing program, the full data set comprised 270 images in each of the three filters.

3. DATA CALIBRATION

The WFC3/IR images have undersampled data at our wavelengths of interest. The DRIZZLEPAC software is the standard tool to improve the resolution of *HST* data, but it is not optimal for high-contrast imaging since it corrects the geometric distortion prior to improving the resolution of the images, the opposite being more appropriate here. We therefore modified the ALICE pipeline (Choquet et al. 2014; Soummer et al. 2014) to include the calibration of dithered WFC3 images.

The program used a nine-point spiral dither pattern with 0.5 pixel dither steps. The *HST* pointing stability within a single orbit for small dithers is ~2–5 mas. Using the WCS information and the "interleave method" (Lauer 1999), the dithered frames were combined to improve the resolution by a factor of 2 (~64 mas pixel^{-1}). The selected dither pattern does not permit reconstruction of two fully independent images using interleaving, and one dithered frame has to be shared between them. The additional time sampling provided by generating two images per nine-point dither meant a deeper contrast and was thus preferred over the case of one image per nine-point dither. The upsampled images are then corrected from the detector distorted frame to an undistorted frame using correction maps (J. Anderson 2015, private communication). Finally, the images were aligned by cross-correlating on the diffraction spikes in the data, resulting in 60 aligned and upsampled images.

The data were reduced using the Karhunen–Loéve Image Projection (KLIP) algorithm based on the principal component analysis (Soummer et al. 2012) used in the ALICE pipeline. For each of the 60 upsampled images, the reference PSF library is assembled imposing a minimum rotation of 2× FWHM at the planet location to reduce self-subtraction.

We assumed knowledge of the location of the planets and reduced the data in local zones around the expected positions for planets b and c, similar to what was done in Soummer et al. (2011). The reduction was performed in annular sections over a parameter space exploring two radial sizes and three azimuthal widths. With ~25 KLIP reductions per image, our parameter space includes ~150 images, giving ~9000 images for each reduction of a given planet/filter combination. We explored a number of geometries and in particular the location of the planet with respect to the zone with the best results when the planet is close to the inner edge of the zone.

Each reduced image is corrected for the KLIP throughput loss using forward modeling, estimated by projecting a *TinyTim* model PSF (Krist et al. 2011) onto the KL modes, as described in Soummer et al. (2012) and Pueyo et al. (2015). We then compute a data quality criterion as the ratio of the algorithm throughput to a noise estimate with matched filtering in a local region around the planet. This criterion is therefore proportional to the true signal-to-noise ratio (S/N), but without introducing any of the planet signal in the calculation so that it does not bias the results by amplifying speckles. The reduced data are ordered according to this criterion and cumulatively combined using a median. The data quality criterion is then recalculated to determine the optimal number of images in the final image, shown in Figure 1. This approach permits exploration of any algorithm parameter space to produce a single final image automatically by identifying the best combination of algorithm throughput and speckle suppression.

Photometry was obtained using matched filtering with a truncated model PSF (5 pixels) to reduce potential contamination from local speckles. This matched filter combined with partial truncation of the planet PSF by the reduction zone leads to an incomplete fraction of the planet flux (~80%). All these effects were carefully calibrated using aperture photometry on archival WFC3 data of white dwarfs (GD153, G191B2B) from *HST* calibration programs and of similar spectral type isolated brown dwarfs. The overall photometric correction precision is of the order of 3%–4%, significantly smaller than the final photometric error bars on the planets.

The PSF library is not rigorously free of companion contribution; however, the contribution of the companion at other roll angles is limited, since the data are not a true ADI sequence (the orientations span 270° over multiple epochs) and the planets are very faint compared to the PSF wings. In addition, the noise has a zero mean within the reduction zone from KLIP but is not necessarily at zero mean within the matched-filter equivalent aperture, and small biases may remain. The validity of the forward modeling approach for this particular data set was investigated by injecting *TinyTim* PSFs in the data at the planets' radial separation over a range of azimuthal angles (25 PSFs for b and 20 PSFs for c). The injected PSF flux was iteratively adjusted to result in the same S/N as each true planet after reduction. The mean photometric error on the synthetic planets was used as a bias correction to account for the two effects discussed above, and the error on the photometry was estimated from the standard deviation in the measured signal for each of the fakes. Upper limit detections for HR8799c in F098M and F139M were obtained by adjusting the injected PSFs to detect almost all of them. To ensure the absence of speckle amplification, we injected "zero-flux synthetic planets" using the exact same pipeline. No significant detection could be found at the location of these injected zero-flux PSFs. Various combinations of reduced images were tested for the presence of flux at given positions as a function of the telescope roll angle and reduction parameters; see Soummer et al. (2011) for a detailed description. We estimated a false positive fraction (FPF) of 7.6×10^{-22} (S/N ~ 10) and 3.8×10^{-7} (S/N ~ 5.3) for b and c in the F127M filter assuming Gaussian statistics. We also calculated an FPF of 2.7×10^{-11} (S/N ~ 7) and 1.3×10^{-4} (S/N ~ 4) for b and c in F127M filter assuming a small number of resolution elements using the Student's *t*-test relation presented in Mawet et al. (2014).

4. RESULTS

Contrast curves for the data in the F127M filter are shown in Figure 2 and indicate the contrast achieved using different analysis techniques and the contrast in the global KLIP and small-zone KLIP reductions. The global KLIP reduction is not used in our analysis; we present this contrast curve estimate to guide future possible studies at high contrast with *HST*/WFC3-IR. The measured VEGAMAG photometry for the detections and 1σ limits is presented in Table 1 using revised zero points.[9] The photometry of the planets is compared with brown dwarfs measured in the same *HST* filters in the color–magnitude

[9] Revised ZP: F098M = 24.2209 mag, F127M = 23.7503 mag, F139M = 23.7679 mag.

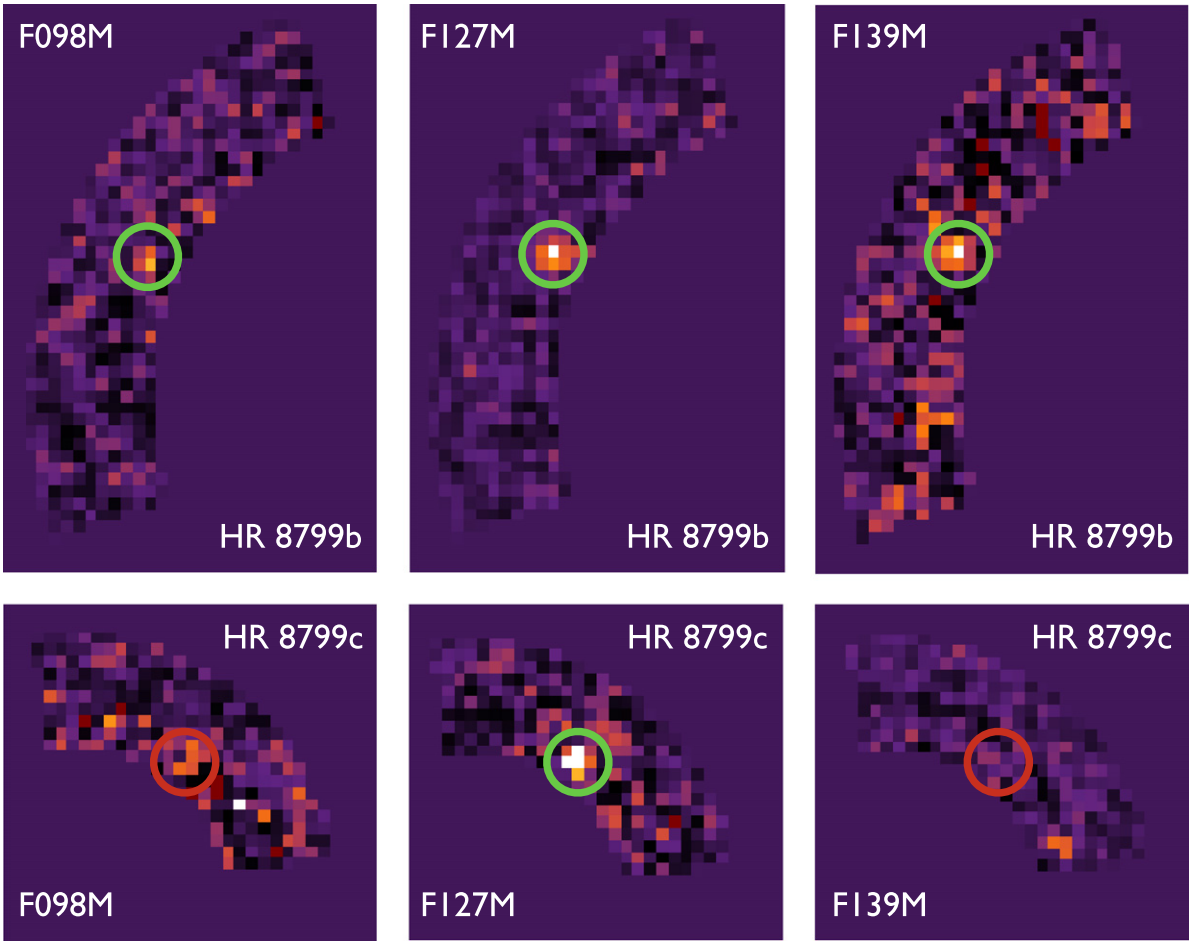

Figure 1. Multi-wavelength *HST*HR8799 data. Top: image zones with locally optimized KLIP detections of HR8799b in all three filters, F098M, F127M, and F139M, respectively. Bottom: same as above, for HR8799c. HR8799c is only detected in the F127M filter, with upper limits in F098M and F139M.

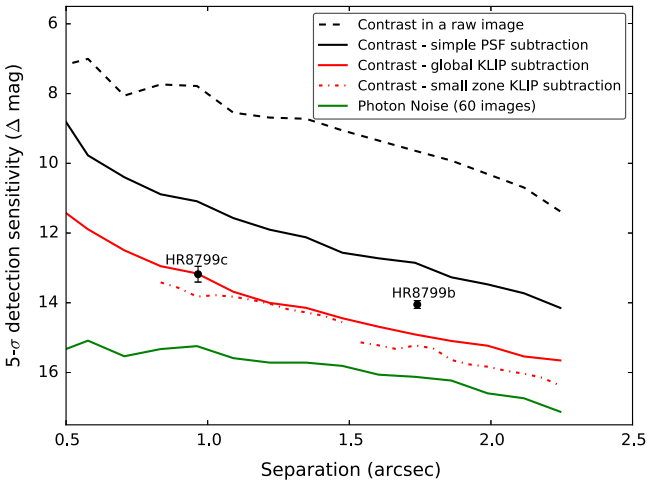

Figure 2. 5σ HR8799 detection sensitivity with ΔF127M magnitudes as a function of angular separation from the star. The black circles are our photometry values for HR8799bc. The solid red line shows the contrast estimated from a global KLIP reduction and the red dashed segments are contrast levels obtained in the optimized zones. This figure is intended to help in the preparation of future observations at high contrast with *HST*/WFC3 with the green line indicating the photon noise floor for the full data set.

diagram in Figure 3. The positions of the planets in Figure 3 verifies that the flux measurement for the planets does not deviate unrealistically from the brown dwarfs. The spectral

Table 1
HR8799bc Absolute Photometry

Planet	*HST* Photometry		
	F098M	F127M[a]	F139M
HR8799b	16.90 ± 0.18	16.20 ± 0.12	17.36 ± 0.26
HR8799c	>15.72	15.38 ± 0.17	>16.16

Note.
[a] The P1640 spectrum through the F127M filter gives HR8799b = 16.16 ± 0.27 and HR8799c = 15.17 ± 0.08.

type derived for each planet is dependent on the contrast between the *J* and water-band fluxes being similar to that measured for brown dwarfs. Using a relation converting *HST* photometric colors to a spectral type from Aberasturi et al. (2014),[10] we calculate a spectral type of L9.5 ± 0.5 for HR8799b and >L7 for HR8799c. The errors are the quadrature sum of the intrinsic scatter in the relation and the error in the photometric color. The larger role of clouds in giant planets with temperatures comparable to cloud-free brown dwarfs complicates the conversion of the color–magnitude position into spectral types. The following two subsections model the combined *HST* photometry with measurements from the

[10] SpT = 1.56–6.25*(F127M–F139M).

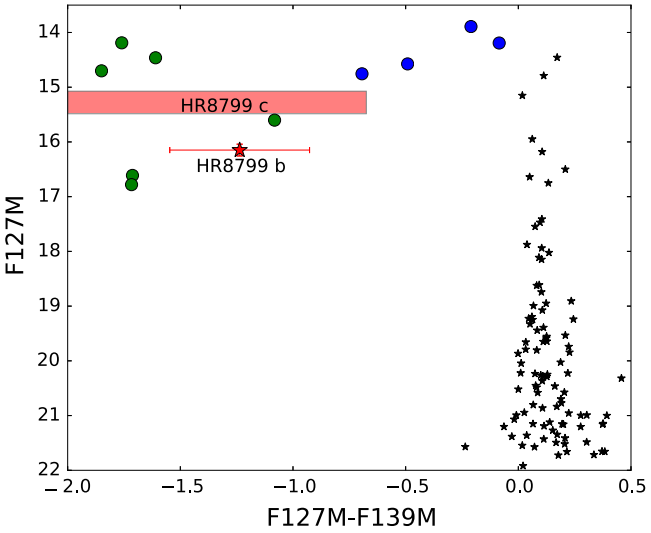

Figure 3. *HST* near-infrared color–magnitude diagram. The HR8799bc planets (red star, shaded region) are plotted with field *L* (blue circles) and *T* (green circles) brown dwarfs from recent *HST* studies (Apai et al. 2013; Aberasturi et al. 2014; Yang et al. 2015). The black points are background field targets. The red rectangle for c represents our upper-limit estimate.

literature at different wavelengths to determine the atmospheric properties.

4.1. HR8799b

The *HST* data in F139M provide the first detection of the planet b in the water absorption region at 1.4 μm. Additionally, the photometric points in F098M and the peak of the *J* band (F127M) are consistent with measurements taken across similar wavelengths with ground-based instruments (Marois et al. 2008; Currie et al. 2011; Oppenheimer et al. 2013). We combine the new *HST* data with photometric data available in the literature and fit the fluxes to synthetic model spectra from Barman et al. (2011, 2015; cited as B15 in the rest of the paper). The models include clouds located at the intersection of the pressure–temperature profile and the chemical equilibrium condensation curve with a parameterized thickness but a homogeneous distribution in latitude and longitude across the planet. The models also include non-equilibrium chemistry for all important C, N, and O bearing molecules, as well as updated line lists for CH4 and NH3 (see B15 for details). The particle size distribution is centered on 5 μm following a log-normal distribution.

Figure 4 (top) shows two fits for the HR8799b photometry, the best fitting model to the F139M (black line), and the best fit to the [4.05] point (Currie et al. 2014, green line). No individual model was able to fit the pair of neighboring fluxes at either F127M and F139M or L' and [4.05]. The discrepancy may indicate missing physical processes in the model and the data are complicated by the non-contemporaneous measurements. Although the [4.05] band covers the Br-α line, accretion is unlikely due to the lack of Br-γ emission in the *K*-band spectrum (Barman et al. 2011). The ratio of F139M flux to F127M flux may be useful for estimating the combined effects of cloud size distribution, cloud thickness, and coverage. However, effective temperature, gravity, and composition will need to be better constrained to avoid degeneracies in the model fitting and better agreement with evolutionary models.

Fitting a combination of near-IR spectroscopy and IR photometry, B15 found a best-matching model with $T_{\rm eff}$ = 1000 K and log(g) = 3.5, with potentially subsolar water abundance and enhanced C/O; however, the uncertain surface gravity results in a wide spread of values, including solar metallicity. In this paper, the cooler best-fit model has solar abundances and we find $T_{\rm eff}$ = 1000–1100 K and log (g) = 3.0–4.5, indicating consistency between photometry-based fits and those including spectroscopy. Our measured water-band flux relative to the *J*-band, however, is brighter than predicted by all of the non-solar models explored by B15, suggesting that perhaps clouds play an important role.

4.2. HR8799c

For HR8799c we measured the photometry in the F127M band, and upper limits were determined for the F098M and F139M filters. The F127M flux is consistent with values obtained by integrating the spectrum from P1640 over the same wavelength range (Oppenheimer et al. 2013), but substantially lower than the reported *J*-band photometry (Marois et al. 2008). The new *HST* data were combined with similar and longer wavelength fluxes from the literature to construct the spectral energy distribution (SED) given in Figure 4 (bottom). Plotted with the data is a model with $T_{\rm eff}$ = 1100 K, log(g) = 3.5, and elevated C/O that fit the *K*-band spectrum from Konopacky et al. (2013). The fits agree well with the *HST* photometry and the longer wavelength data with the exception of a significant difference with the earliest measurement of the *J*-band photometry and an $\sim$2.5σ difference with the [4.05] data point. Our models for HR8799c with homogeneous cloud modeling agree, within the uncertainties, with the *HST* photometry and longer wavelength data out to $\sim$3.5 μm with the exception of the first epoch of *J*-band photometry.[11] The difficulty in fitting all available photometry with reported uncertainties persists even when using patchy cloud models formed by combining clouds at different temperatures (Skemer et al. 2014) or opacity (Currie et al. 2014), and the *HST*F127M measurement is more consistent with the patchy cloud models. Our attempts with a linear combination of models did not provide a better fit than the homogeneous cloud model with higher C/O ratio presented in Figure 4 (bottom).

5. DISCUSSION

Among the *HST* filters, F127M is the most analogous to a ground-based filter and can be directly compared to previous results reported in the *J*-band. The HR8799b F127M photometry is consistent with previous results (Marois et al. 2008). There are two prior reported values for HR8799c—a P1640 spectrum (Oppenheimer et al. 2013) and a Keck *J*-band flux (Marois et al. 2008). The ground-based *J*-band photometry for HR8799c is approximately twice as bright as the measured *HST* flux. Integrating the HR8799c flux calibrated P1640 spectrum through the F127M filter matches the *HST* photometry to within 2σ. A potential solution for this discrepancy might be intrinsic photometric variability caused by heterogeneous cloud layers, which we find is not required in our model fits. The early ground-based photometry might also have suffered from calibration issues, which, combined with the

[11] Improved analysis techniques and stellar variability cannot account for the factor of two difference in flux.

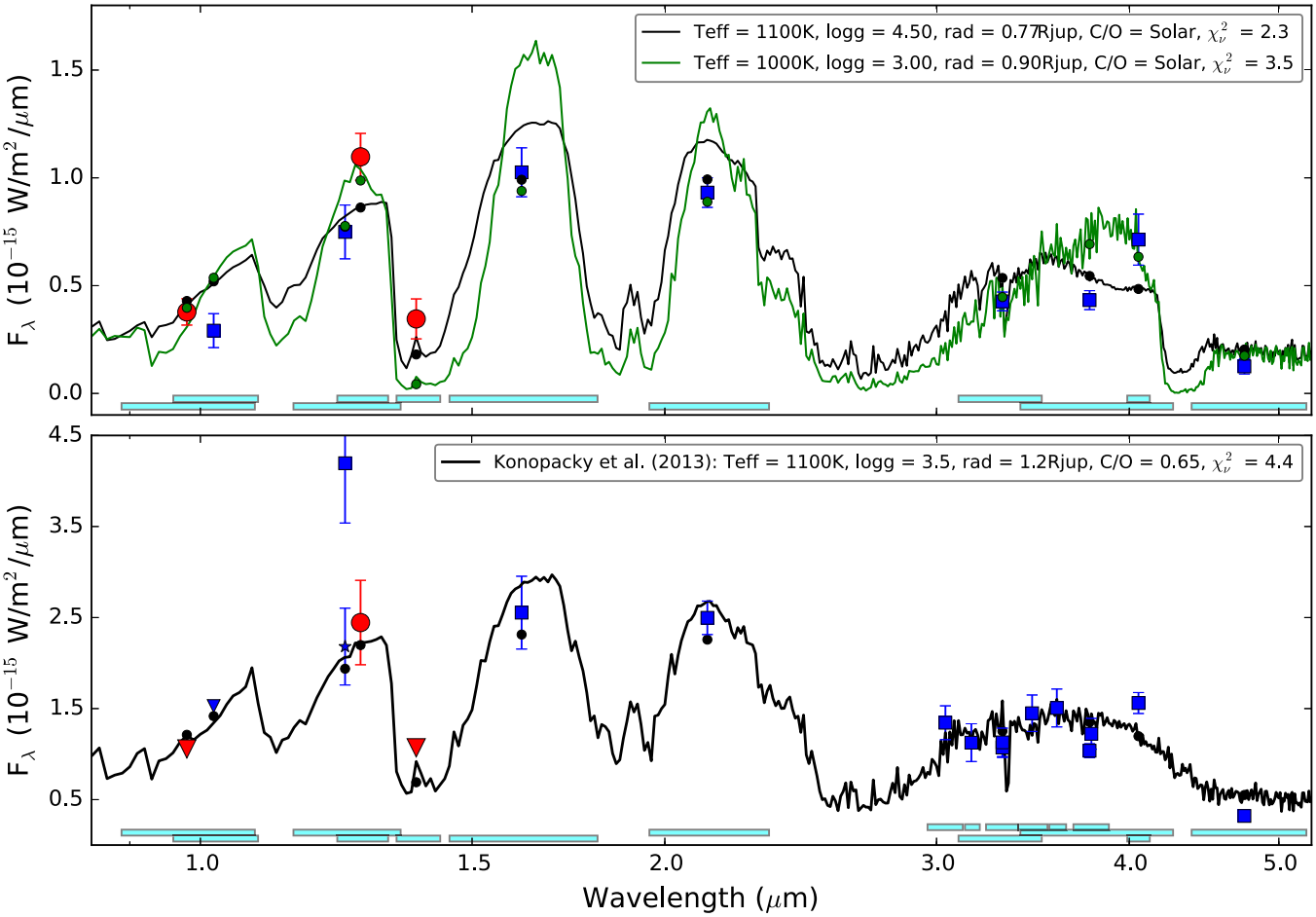

Figure 4. Top: model fits to HR8799b data. In the figure the red circles are *HST* photometry, and the blue squares are ground-based photometry, with the filter width shown as cyan bars at the bottom of the plot. The black and green lines (and corresponding circles) are the model spectra fitted to the full data set. Bottom: the black line is the Konopacky et al. (2013) HR8799c model. The ground-based photometry in this paper comes from Marois et al. (2008), Currie et al. (2011), Oppenheimer et al. (2013), Currie et al. (2014), Skemer et al. (2012), Skemer et al. (2014), and Galicher et al. (2011). The blue star for HR8799c is the *J*-band photometry from Oppenheimer et al. (2013).

intrinsic variability of the star, might explain some of the difference in flux measurement.

Efforts to match synthetic spectra to the ensemble of photometric data for HR8799b result in high effective temperatures and corresponding radii that are smaller by ∼50% (0.69–0.92 $R_{\rm Jup}$) than predicted by theoretical brown dwarf and giant planet cooling tracks (see Marley et al. 2012 for a summary). Difficulty finding a model spectrum that simultaneously matches the near- and mid-IR photometry could be due to the non-contemporaneous nature of the observations, or perhaps the model–observation inconsistencies at multiple bands are an indication of large-scale flux variations. Large variability would bias such model comparisons. For example, the bright *J*-band flux from Marois et al. (2008) is more consistent with higher effective temperatures than our *HST*F127M flux. The deep water absorption demonstrates that the atmospheres of both b and c are not enshrouded in high altitude hazes or clouds many pressure scale heights thick, important for many transiting exoplanets (Kreidberg et al. 2014). Nonetheless, clouds are important in shaping the overall SED of the planets. Both best-matching models plotted in Figure 4 (top panel) have clouds composed primarily of iron and magnesium-silcate grains, located in the near-IR photosphere. The cooler model has a cloud located at $P_{\rm gas} \sim 1$ bar and extending upward 1 pressure scale height. The warmer (and higher gravity) model has a cloud base near 10 bar, extending upward 2 pressure scale heights. Using single models to reproduce the observations assumes global cloud coverage, which is probably an overestimation.

With SEDs well sampled observationally and with model spectra that match reasonably well, the bolometric luminosities of both planets can be estimated, and we determine $L_{\rm bol}$ values of -5.1 ± 0.1 for b and -4.7 ± 0.1 for c, consistent with Marois et al. (2008).

6. CONCLUSIONS

In this study, we have demonstrated that WFC3 is capable of investigating the atmospheres of planets requiring high contrast at wavelengths either inaccessible from the ground or at which the extreme adaptive optics systems perform poorly. With its photometric stability, *HST* provides a valuable resource to explore exoplanet atmospheres and will enable measurements such as the search for atmospheric variability. The data from the current program can be used to build a PSF library for future high-contrast imaging programs. Based on experience from the current program, future studies would benefit from obtaining more exposures rather than performing the time-consuming in-orbit roll.

In this study, we were able to detect HR8799b in three WFC3 filters. In this work and in other studies, matching all of the data simultaneously has not been possible. In particular, some of the shortest wavelength data favor warmer conditions while some of the longer wavelength IR data favor cooler conditions, possibly caused by clouds. For HR8799c, we find very good agreement between the model fit with the F127M, resolving the longstanding difficulty of fitting the previously reported *J*-band photometry. A possible explanation for the F127M and *J*-band flux difference is variability. Future spectrophotometric monitoring of HR8799b and HR8799c in the near- and mid-IR might resolve whether the planets are variable over the duration of a single rotation period.

Based on observations made with the *Hubble Space Telescope*, associated with program #12511. This research was supported in part by NASA cooperative agreements HST-GO-12511.04, HST-AR-12652.01, and NSF AST-1411868.

REFERENCES

Aberasturi, M., Burgasser, A. J., Mora, A., et al. 2014, AJ, 148, 129
Apai, D., Radigan, J., Buenzli, E., et al. 2013, ApJ, 768, 121
Barman, T. S., Konopacky, Q. M., Macintosh, B., & Marois, C. 2015, ApJ, 804, 61
Barman, T. S., Macintosh, B., Konopacky, Q. M., & Marois, C. 2011, ApJ, 733, 65
Burrows, A., Hubbard, W. B., Lunine, J. I., & Liebert, J. 2001, RvMP, 73, 719
Charbonneau, D., Allen, L. E., Megeath, S. T., et al. 2005, ApJ, 626, 523
Charbonneau, D., Brown, T. M., Noyes, R. W., & Gilliland, R. L. 2002, ApJ, 568, 377
Chauvin, G., Lagrange, A.-M., Dumas, C., et al. 2005a, A&A, 438, L25
Chauvin, G., Lagrange, A.-M., Zuckerman, B., et al. 2005b, A&A, 438, L29
Choquet, É, Pueyo, L., Hagan, J. B., et al. 2014, Proc. SPIE, 9143, 57
Currie, T., Burrows, A., Girard, J. H., et al. 2014, ApJ, 795, 133
Currie, T., Burrows, A., Itoh, Y., et al. 2011, ApJ, 729, 128
Deming, D., Brown, T. M., Charbonneau, D., Harrington, J., & Richardson, L. J. 2005, ApJ, 622, 1149
Galicher, R., Marois, C., Macintosh, B., Barman, T., & Konopacky, Q. 2011, ApJL, 739, L41
Knutson, H. A., Charbonneau, D., Allen, L. E., et al. 2007, Natur, 447, 183
Konopacky, Q. M., Barman, T. S., Macintosh, B. A., & Marois, C. 2013, Sci, 339, 1398
Kreidberg, L., Bean, J. L., Désert, J.-M., et al. 2014, Natur, 505, 69
Krist, J. E., Hook, R. N., & Stoehr, F. 2011, Proc. SPIE, 8127, 0
Kuzuhara, M., Tamura, M., Kudo, T., et al. 2013, ApJ, 774, 11
Lagrange, A.-M., Bonnefoy, M., Chauvin, G., et al. 2010, Sci, 329, 57
Lauer, T. R. 1999, PASP, 111, 1434
Marley, M. S., Saumon, D., Cushing, M., et al. 2012, ApJ, 754, 135
Marois, C., Lafrenière, D., Doyon, R., Macintosh, B., & Nadeau, D. 2006, ApJ, 641, 556
Marois, C., Macintosh, B., Barman, T., et al. 2008, Sci, 322, 1348
Marois, C., Zuckerman, B., Konopacky, Q. M., Macintosh, B., & Barman, T. 2010, Natur, 468, 1080
Mawet, D., Milli, J., Wahhaj, Z., et al. 2014, ApJ, 792, 97
Oppenheimer, B. R., Baranec, C., Beichman, C., et al. 2013, ApJ, 768, 24
Pueyo, L., Soummer, R., Hoffmann, J., et al. 2015, ApJ, 803, 31
Rameau, J., Chauvin, G., Lagrange, A.-M., et al. 2013, ApJL, 772, L15
Sing, D. K., Vidal-Madjar, A., Désert, J.-M., Lecavelier des Etangs, A., & Ballester, G. 2008, ApJ, 686, 658
Skemer, A. J., Hinz, P. M., Esposito, S., et al. 2012, ApJ, 753, 14
Skemer, A. J., Marley, M. S., Hinz, P. M., et al. 2014, ApJ, 792, 17
Soummer, R., Brendan Hagan, J., Pueyo, L., et al. 2011, ApJ, 741, 55
Soummer, R., Perrin, M. D., Pueyo, L., et al. 2014, ApJL, 786, L23
Soummer, R., Pueyo, L., & Larkin, J. 2012, ApJL, 755, L28
Yang, H., Apai, D., Marley, M. S., et al. 2015, ApJL, 798, L3
Zuckerman, B., Rhee, J. H., Song, I., & Bessell, M. S. 2011, ApJ, 732, 61